Effect of turbulent kinetic energy dissipation rate on the prediction of droplet size distribution in stirred tanks

Effect of Turbulent Kinetic Energy Dissipation Rate on the Prediction of Droplet Size Distribution in Stirred Tanks

Francesco Maluta[1*], Antonio Buffo[2], Daniele Marchisio[2], Giuseppina Montante[1], Alessandro Paglianti[3], Marco Vanni[2]

[1]Dipartimento di Chimica Industriale 'Toso Montanari', Alma Mater Studiorum – Università di Bologna, Bologna, Italy

[2]Dipartimento Scienza Applicata e Tecnologia, Politecnico di Torino, Torino, Italy

[3]Dipartimento di Ingegneria Civile, Chimica, Ambientale e dei Materiali, Alma Mater Studiorum – Università di Bologna, Bologna, Italy

*C*orresponding author:*

francesco.maluta@unibo.it

Dipartimento di Chimica Industriale "Toso Montanari", Via Terracini 34, 40131 Bologna, Italy

Keywords: Liquid-Liquid; Stirred Tanks; Turbulence; Population Balance; CFD; PIV

Abstract:

In this work the capabilities of Two Fluid Model simulations coupled with a Population Balance Model solved with the Quadrature Method of Moments in predicting the turbulent kinetic energy dissipation rate and the droplet size distribution in a dilute liquid-liquid stirred tank are investigated. For a strict evaluation of the numerical and modelling approximations, original two-phase flow fields and droplet size distributions are collected by Particle Image Velocimetry and a laser diffraction technique, respectively. The spatial discretization requirements for achieving grid independent and reliable predictions of the turbulent variables already observed in RANS-based simulations of single-phase stirred tanks are confirmed also for the investigated dilute two-phase system, for which the effect of the dispersed phase on the continuous liquid is negligible. Besides, better prediction of the droplet size distribution is apparently obtained with poorly predicted turbulent kinetic energy dissipation rate, showing that the usually adopted parameters of the breakup kernel have been tuned for coarse grids. A way to derive grid independent breakup kernel parameters and a correction based on the spatial distribution of turbulent dissipation rate are proposed to account for the underestimation of the turbulent variables in the RANS simulation of industrial scale equipment.

1 Introduction

Several operations in the food, pharmaceutical and chemical industry rely on turbulent dispersions of immiscible liquids. Emulsification, organic synthesis and extractions, among the others, are heavily dependent on the properties of the dispersion which rheology, stability and exchange properties are determined by many factors, one of the most important being the drop size distribution (DSD) of the disperse phase (Afshar Ghotli et al., 2013; Leng and Calabrese, 2016). The DSD, in fact, has an important role in governing the fluid dynamics and the inter-phase mass transfer in the equipment, that in turn usually affect the performances of the whole operation (Afshar Ghotli et al., 2013; Drumm et al., 2009; Maaß et al., 2012).

Computational models have become an important aid in predicting the equipment fluid dynamics and the evolution of the DSD. Among the different modelling approaches, e.g. fully-resolved (Derksen and Van Den Akker, 2007; Di Miceli Raimondi et al., 2008), Lagrangian point-particle (Jaworski and Pianko-Oprych, 2002; Rieger et al., 1996) and Two-Fluid Model (TFM) (Gao et al., 2016; Hu et al., 2015), TFM methods have the advantage of being computationally cheaper than the others, but, at the same time, they do not allow to evaluate the distribution of the disperse phase properties, such as size, velocity, interfacial properties, that are instead described with a unique value for each disperse element (Buffo et al., 2013). To overcome this limitation, the distribution of the internal

properties of interest can be described by means of a population balance model (PBM) that can be solved in a computational fluid dynamics (CFD) framework (Marchisio and Fox, 2013; Shiea et al., 2020).

Fully predictive CFD-PBM models require reliable closure equations to account for coalescence and breakage. Although in recent times there have been attempts to derive coalescence and breakage models, usually called kernels, starting from detailed numerical simulations (Amani et al., 2019; Karimi and Andersson, 2020; Mukherjee et al., 2019), the models commonly adopted to describe these mechanisms are mostly phenomenological, in which heavy simplifications and approximations are often made (Liao and Lucas, 2010, 2009). However, recently there has been a significant effort to improve the kernels theoretical formulation, especially the relationship between fluid particles and turbulence (Karimi and Andersson, 2020; Solsvik et al., 2016) and high-order turbulence effects like intermittency (Baldyga and Podgórska, 1998; Gao et al., 2016; Li et al., 2017a; Podgórska, 2005; Podgórska and Bałdyga, 2001), but the computational requirements needed to solve these kernels remains unaffordable for large scale equipment (Castellano et al., 2019). Coalescence and breakage kernels usually contain information regarding both the fluid dynamics and the physical properties of the investigated system, together with scalar parameters that include all the modelling uncertainties (Falzone et al., 2018). These scalar parameters are not universal constants, as they should be if the model fully described the physics of the problem, but they are often tuned on the specific systems in order to

minimize the distance between experimental data and model predictions (Azizi and Taweel, 2011; Bakker et al., 2001; Castellano et al., 2019). It is important to remark that the fitting procedures usually adopted in the literature make use of important simplifications of the experimental flow features, one of the most important being the turbulent dissipation rate field, consisting in either just one value representative of the whole field or a small collection of values to describe the inhomogeneities. By means of example, Coulaloglou and Tavlarides, (1977) assumed that the impeller region of a stirred tank is where breakage predominates and a single value of the turbulent dissipation rate was used, equal to 70 times the volume averaged value. Narsimhan et al., (1979) adopted the same criterion, but used a reduced value of the turbulent dissipation rate in the impeller zone, equal to 30 times the averaged turbulent dissipation rate, derived from an average in the impeller discharge jet. Alopaeus et al., (2002) derived the kernel parameters through a multi-block subdivision of a stirred tank (Alopaeus et al., 1999) based on a previous experimental work (Bourne and Yu, 1994) that reported a value of turbulent dissipation rate in the impeller region equal to 33.8 times the global volume average. These examples highlight that the kernel parameter values reported in the literature are intrinsically dependent on the experimental data fitting, and they are determined by the assumed turbulent dissipation rate fields.

Thus, the turbulent kinetic energy dissipation rate has a major effect in determining the ratio between breakage and coalescence rates as well as the evolution of the droplets size (Li et al., 2017b). Coroneo et al., (2011) proved that, in the simulations of single-phase

stirred tanks based on Reynolds Averaged Navier Stokes equations, the underprediction of turbulent variables were in fact caused by insufficiently fine grids and low order numerical schemes. Jaworski et al., (2007) pointed out the importance of a correct calculation of the turbulent quantities in the prediction of the DSD and how their underestimation led to larger droplets diameters. Other authors acknowledged and identified the issue of underestimating the turbulent dissipation rate because of a coarse mesh and low order numerical schemes, either without proposing alternative solutions (Drumm et al., 2009; Tang et al., 2018; Zhang et al., 2012), by quantifying the error on the turbulent variables and how this affected their results (Alopaeus et al., 2002; Kálal et al., 2014), or deriving new experimental-numerical hybrid methods tuned to correctly predict the DSD (Khajeh Naeeni and Pakzad, 2019). Recently, the introduction of a uniform scalar correction in the kernels has been proposed (Gao et al., 2016; Li et al., 2017b) for taking into account the underprediction of the turbulent dissipation field.

In this work, for the first time an in-depth analysis of the effects related to the underprediction of the turbulent dissipation rate and to the uncertainties tied to the kernel parameters values on the resulting DSD and breakup events is carried out by studying a liquid-liquid stirred tank from both experimental and numerical point of view. A single operating condition in a very dilute liquid-liquid stirred tank is experimentally investigated (volume fraction of 0.1%), in such a way to neglect coalescence and to focus on the drop breakage. The dispersed phase effect on the continuous phase turbulent flow field is

assessed by purposely collected experimental measurements of both local velocity profiles and droplet size distributions. On the numerical side, first the quality of the turbulent kinetic energy dissipation rate and velocity field predictions obtained by the CFD-PBM approach is assessed. Particular attention is devoted to the evaluation of a grid-independent turbulent flow field, as an essential starting point to analyze the breakage frequency distribution in the stirred tank and explore the effects of the turbulent fluid dynamics on the breakage frequency at the equipment scale in mechanically stirred tanks. Then a comparison between experimental and numerical DSD is performed to evaluate the quality of the breakup kernel predictions and to identify the uncertainties associated with the kernel parameters using a quantitative approach, highlighting the importance of a proper fluid dynamics description. To the best of the authors knowledge, in this work for the first time the application of a CFD-PBM approach is studied by focusing on both fluid dynamics and DSD predictions and their validation with the experimental data.

The outline of the paper is the following. The experimental set-up is described in Section 2. The fluid dynamics model equations are presented in Section 3, together with the population balance model, whilst the numerical solution procedure and the coupling between fluid dynamics and population balance equation is presented in Section 4. The numerical solution grid independence study is presented in Section 5. In section 6, the results of the comparison between experiments and simulations are shown. In section 7, a

grid dependent scalar correction for the breakup kernel is proposed, with the purpose to reduce computational simulation time of large-scale equipment.

In this work the interconnections between turbulent fluid dynamics and drop breakage in mechanically stirred tanks are evaluated by means of a RANS TFM PBM approach, whose predictions are validated by experimental results, both original and from the literature. Local and global experimental results were used to compare grid independent turbulent variables, that allowed to investigate the spatial distribution of breakup frequency. The resulting DSD predicted by the model is compared with purposely collected experimental distributions and the comparison underlines the dependency of the breakup kernel parameters on the spatial distribution of the turbulent flow field used in the tuning conditions.

2 Experimental set-up

The investigated stirred tank was previously employed in liquid-liquid investigations (Laurenzi et al., 2009; Maluta et al., 2020). It consists of a cylindrical, flat bottomed tank with diameter, T, and height, H_T, both equal to 0.232m. It was equipped with four equally spaced baffles of width equal to $T/10$. A single Rushton turbine (RT) mounted on a central shaft was used for agitation. The diameter of the impeller, D, was equal to 0.077m, corresponding to a D/T ratio equal to 1/3, and the off-bottom clearance, C, was half the

vessel diameter (*C/T* =1/2). The liquid height, H_L, was always maintained at H_T, corresponding to a total volume of 9.8L.

The two immiscible liquids were commercial diesel fuel with density, ρ_D, equal to 810kg/m^3, viscosity, μ_D, equal to 3.5×10^{-3}Pa·s and surface tension of 27.6mN/m (measured at room temperature) and demineralized water with density, ρ_C, and viscosity, μ_C, equal to 998kg/m^3 and 10^{-3} Pa·s respectively.

The experiments were carried out after the injection of 9.7mL of diesel fuel in the stirred vessel filled with demineralized water, corresponding to a volume fraction of $\alpha_D = 10^{-3}$, at an impeller rotational speed, *N*, of 500rpm, to ensure complete dispersion. Under this agitation condition, the flow regime is fully turbulent being the rotational Reynolds number, $Re = \rho_C N D^2 / \mu_C$, equal to 4.9×10^4. The injection of the disperse phase occurred in the proximity of the impeller by means of a rigid needle.

The local measured data were referred to a cylindrical coordinate system, with the origin placed on the centre of the tank bottom, the radial coordinate, *r*, positive if directed toward the vessel wall and the axial coordinate, *z*, positive if directed upwards.

The drop size distribution was measured by means of a Spraytec laser diffraction system (Malvern Panalytical) equipped with a wet sample dispersion unit. The Spraytec laser diffraction system measures the intensity of light scattered as a laser beam passes through a dispersion. Light intensity is collected by several detectors that measure the intensity of light scattered by the droplets over a wide range of angles. The set of light intensities is

then analyzed to calculate the size of the droplets in the sample that created the scattering pattern. The sampling was performed after 40 minutes from the oil injection, to make sure that the system was at the steady state. A 100mL sample of the mixture was withdrawn from the system midway between two consecutive baffles at a position of $r/T = 0.35 \pm 0.02$, $z/T = 0.69 \pm 0.04$ with a plastic tube of 6mm diameter not to alter the DSD. A single sample point was used since the DSD is expected to have a rather constant shape throughout the tank with little variations on the mean parameters of the distribution (Zhou and Kresta, 1998a). The sample was promptly transferred to a *wet sample dispersion unit* (Malvern Panalytical) that uses a small stirrer to continuously recirculate the sample through a measurement cell positioned between the Spraytec transmitter and receiver units. An insufficient rotational speed of the wet dispersion unit stirrer would not circulate the larger drops, whereas an excessive rotation could break the droplets. Both these effects would alter the DSD. The influence of the wet sample dispersion unit recirculation flow rate, the sample volume and measuring time on the DSD were carefully quantified at the beginning of the experimental campaign. The time evolution of the scattering pattern is tracked for about 30s, and data are averaged on a 10s window, observing very few variations in the observed time window. The size of the droplets that created the scattering pattern was calculated, producing a discretized DSD in term of the weighted volume fractions with respect to the total disperse phase volume in the sample. Triballier et al. (2003) analyzed the performances of Spraytec and the possible sources of errors. They pointed out one of

the strengths of Spraytec is that the Lorenz-Mie theory is employed allowing the correct measurements of very fine sprays. Triballier et al. (2003) also argued that the correction suggested by Malvern for solving the problem of the multiple scattering seems to induce relevant errors. It is worthwhile noticing that this drawback does not influence the accuracy of the present measurements because our experiments were performed at obscuration up to 10% that is absolutely lower than the critical value of 60% above which the multiple scattering has to be taken into account.

The flow fields of the diesel fuel droplets and of the continuous phase with and without droplets were measured by Particle Image Velocimetry (PIV), similarly to previous investigations concerning gas-liquid (Montante et al., 2008) and solid-liquid (Montante et al., 2012) stirred tanks. Data were collected on a portion of the vertical plane located midway between two consecutive baffles, with $0<r/T<0.5$ and $0.3<z/T<0.7$. Water was seeded with polymeric particles coated with fluorescent Rhodamine B that emit the received laser light at the wavelength of 590nm, while the droplets have the same emission wavelength as the laser light. By using two cameras equipped with optical filters, each camera received the proper light signal. The pulsed Nd:YAG laser (λ=532nm, 65mJ) and the two Charge-Coupled Device cameras (resolution of 1344×1024 pixels) were handled by a Dantec Dynamics synchronization and acquisition system. The areas viewed from the two cameras were identical.

The instantaneous velocity vectors were obtained from the cross-correlation of images collected in double-frame mode. The time interval between the two laser pulses was set to 270μs, the total number of image pairs was 2000. A vector resolution of 1.7mm was obtained by applying the cross-correlation on an interrogation area size of 32×32 pixels with on overlap of 50%. The instantaneous vectors were discarded if they did not fulfil two conditions, one based on the evaluation of the peak heights in the correlation plane and the other on the velocity magnitude, as previously done for dilute solid-liquid systems (Montante et al., 2012). The PIV uncertainty has been evaluated following the approach suggested by Sciacchitano and Wieneke (2016) based on Montecarlo simulations, the uncertainty in the velocity measurements is between 2-3%.

The instantaneous velocities were ensemble averaged to obtain the mean axial and radial velocity components, U and V, and the axial and radial root mean square (RMS) velocity fluctuations, u' and v'.

3 Computational model

The simulations were based on the RANS-TFM equations written for two incompressible fluids under isothermal conditions. The disperse phase continuity and momentum equations specifically solved in this work are the following:

$$\frac{\partial(\alpha_D \rho_D)}{\partial t} + \nabla \cdot (\alpha_D \rho_D \boldsymbol{u_D}) = 0 \quad (1)$$

$$\frac{\partial(\alpha_D \rho_D \boldsymbol{u_D})}{\partial t} + \nabla \cdot (\alpha_D \rho_D \boldsymbol{u_D u_D}) = -\alpha_D \nabla P + \alpha_D \rho_D \boldsymbol{g} + \nabla \cdot (\boldsymbol{\tau_D} + \boldsymbol{\tau^t}) + \boldsymbol{F} \quad (2)$$

Where α_D is the volume fraction of the disperse phase, $\boldsymbol{u_D}$ is the disperse phase mean velocity vector, P is the pressure, $\boldsymbol{g}$ is the gravity vector and $\boldsymbol{\tau_D}$ is the viscous stress tensor. The Reynolds stress tensor, $\boldsymbol{\tau^t}$, and the interphase momentum transfer term, $\boldsymbol{F}$, need to be modelled to mathematically close the set of equations.

The continuity and momentum conservation equations for the continuous phase are in the same form of Eq. (1) and Eq. (2).

The Reynolds stress tensor was modelled with the single-phase standard *k*-*ε* turbulence model with the properties of the continuous phase, as already done for similar systems (Gao et al., 2016; Li et al., 2017a):

$$\frac{\partial \alpha_C \rho_C k}{\partial t} + \nabla \cdot (\alpha_C \rho_C k \boldsymbol{u_C}) = \nabla \cdot \left(\alpha_C \frac{\mu_t}{\sigma_k} \nabla k\right) + 2\alpha_C \mu_t \boldsymbol{E^2} - \alpha_C \rho_C \varepsilon \quad (3)$$

$$\frac{\partial \alpha_C \rho_C \varepsilon}{\partial t} + \nabla \cdot (\alpha_C \rho_C \varepsilon \boldsymbol{u_C}) = \nabla \cdot \left(\alpha_C \frac{\mu_t}{\sigma_\varepsilon} \nabla \varepsilon\right) + \alpha_C C_{1\varepsilon} \frac{\varepsilon}{k} 2\mu_t \boldsymbol{E}^2 - \alpha_C C_{2\varepsilon} \rho_C \frac{\varepsilon^2}{k} \quad (4)$$

Where α_C and ρ_C are the volume fraction and the density of the continuous phase, respectively, k is the turbulent kinetic energy, ε is the turbulent dissipation rate, $\boldsymbol{E}$ is the rate of deformation tensor and $\mu_t = \rho_C \mathrm{C}_\mu \, k^2/\varepsilon$ is the turbulent viscosity. The five model constants σ_k, σ_ε, $C_{1\varepsilon}$, $C_{2\varepsilon}$ and C_μ assume their standard values of 1.00, 1.30, 1.44, 1.92 and 0.09, respectively.

The inter-phase momentum transfer term consisted in the drag force only, $\boldsymbol{F}_{drag,CD}$, that was considered prevailing over the other interfacial forces acting between the phases (such as lift force, turbulent dispersion, wall lubrication), as in similar dilute liquid-liquid stirred tanks (Gao et al., 2016; Li et al., 2017a). The drag force was written in the form:

$$\boldsymbol{F}_{drag,CD} = \frac{3}{4}\frac{\alpha_D}{d_D} C_D \rho_C \|\boldsymbol{u_D} - \boldsymbol{u_C}\|(\boldsymbol{u_D} - \boldsymbol{u_C}) \quad (5)$$

In Eq.(5), d_D is the droplet diameter and C_D is the drag coefficient calculated with the well-known Schiller & Naumann correlation:

$$C_D = 24\left(1 + 0.15Re_p^{0.687}\right)/Re_p \quad (6)$$

With the drop Reynolds number, Re_p, defined as:

$$Re_p = \frac{\|\boldsymbol{u_D} - \boldsymbol{u_C}\| d_D \rho_C}{\mu_C} \quad (7)$$

valid for $0.1 < Re_p < 1000$.

As a matter of fact, the drag force magnitude acting on a droplet depends on the drop diameter. When the drop size distribution of the population of droplets is relatively narrow, a widely accepted hypothesis is to consider that all the droplets move with the same mean velocity (Gao et al., 2016). The resulting drag force is based on a single diameter value equal to the Sauter mean diameter of the population (Buffo and Marchisio, 2014). Since the Sauter mean diameter can be defined as the ratio between the third and the second order moment of the DSD, the DSD moments are required to close the system of equations.

3.1Population Balance Model

The PBM for the system under study consists of a population balance equation (PBE), with the droplet size being the internal coordinate of the disperse phase. When the disperse phase volume fraction is small, a common assumption is to neglect the coalescence events (Maaß et al., 2012; Marchisio and Fox, 2013; Wang and Calabrese, 1986). In fact coalescence can become significant for clean systems at dispersed phase volume fractions larger than 0.05, while it is usually neglected for volume fractions smaller than 0.01 (Leng and Calabrese, 2016). When the momentum transfer due to collisions between droplets can be neglected, when no growth mechanisms exists, the PBE becomes:

$$\frac{\partial n(d_D)}{\partial t} + \nabla \cdot (n(d_D)\boldsymbol{u_D}) = \int_{d_D}^{\infty} \beta(d_D, d')g(d')n(d')\mathrm{d}d' - g(d_D)n(d_D) \qquad (8)$$

Where $n(d_D)$ is the DSD and the term on the right-hand side of the equation is a source term that accounts for the discontinuous changes due to breakup.

In Eq.(8) g is the breakup kernel expressing the breakup frequency and $\beta(d_D, d')$ is the daughter distribution function that gives the size distribution of drops originating from the breakage of a drop of diameter d'. In this work the daughter distribution function proposed by Laakkonen et al. (2006) was used due to its low computational cost and the fair agreement with more detailed models (Li et al., 2017a). The daughter distribution function has the following expression (Laakkonen et al., 2006):

$$\beta(d_D, d') = 180\left(\frac{d_D^2}{d'^3}\right)\left(\frac{d_D^3}{d'^3}\right)^2\left(1-\frac{d_D^3}{d'^3}\right)^2 \quad (9)$$

Eq. (9) assumes binary breakage based on a beta distribution, in which symmetric breakup is considered as the event with the highest probability. The binary breakage assumption is reasonable due to the expected small size of the droplets and the low viscosity of the disperse phase (Li et al., 2017b).

The Alopaeus breakup kernel (Alopaeus et al., 2002) was used in this work. The kernel assumes a Poisson point process distribution frequency of the eddy-drop collisions in which the turbulent dissipation rate, ε, affects said frequency. Its expression is:

$$g = C_1\varepsilon^{1/3}erfc\left(\sqrt{\frac{C_2\sigma}{\rho_C\varepsilon^{2/3}d_D^{5/3}}+\frac{C_3\mu_D}{\sqrt{\rho_C\rho_D}\varepsilon^{1/3}d_D^{4/3}}}\right) \quad (10)$$

With C_1, C_2, C_3 being model constants and σ being the water-diesel fuel interfacial tension equal to 44.7mN/m, estimated for biodiesel-diesel fuel blends. The constant values were taken equal to 3.68, 0.0775 and 0.2, respectively, being the values for C_1 and C_3 the original values proposed by Alopaeus et al. (2002) and the value for C_2 being fitted with experimental data for a similar system by Li et al. (2017a).

In this work, the Quadrature Based Method of Moment (QMOM) was adopted to solve Eq.(8). With this approach, the NDF is simplified with a quadrature approximation:

$$n \approx \sum_{i=1}^{N_q} w_i\delta[d_D - d_i] \quad (11)$$

where N_q is the order of the approximation, w_i are the quadrature weights and d_i are the nodes or abscissas of the quadrature. The quadrature nodes and weights are obtained

from the first 6 moments $(M_0, M_1, \dots, M_5)$ of the NDF using the well-known Product-Difference algorithm, as described by Marchisio & Fox (Boccardo et al., 2019; Marchisio and Fox, 2013; Shiea et al., 2020), analogously to what already done by Buffo et al. (2012) for gas-liquid systems following a sensitivity analysis on the number of nodes for the quadrature approximation to assess the accuracy of the approximation. Substituting the quadrature approximation of the moment of order k in the moment transport equation one obtains:

$$\frac{\partial M_k}{\partial t} + \nabla \cdot (M_k \boldsymbol{u_D}) = \sum_{i=1}^{N_q} w_i g(d_i) \left[\int_0^\infty \beta(d_D, d_i) d_D^k \mathrm{d}d_D\right] - d_i^k \qquad (12)$$

Where the integral between square brackets is analytically solved, once Eq. (9) is substituted into the term in square brackets of Eq. (12), resulting in:

$$\int_0^\infty \beta(d_D, d_i) d_D^k \mathrm{d}d_D = \frac{3240 d_i^k}{(k+9)(k+12)(k+15)} \qquad (13)$$

4 Numerical solution procedure

The Two Fluid Model equations were solved with a modified version of the OpenFOAM 5.0 solver `twoPhaseEulerFoam` and the default OpenFOAM merged PISO-SIMPLE algorithm (PIMPLE) detailly described by Passalacqua and Fox (2011) in a computational domain coincident with the experimental stirred tank, that was built with ANSYS Design-Modeler and discretised with hexahedral elements generated with ANSYS

ICEM. The rotation of the impeller was accounted for with the unsteady formulation of the so-called Multiple Reference Frame approach (MRF). The boundary conditions and the order of the numerical schemes used for each variable are reported in Tab. 1 and Tab. 2, respectively.

Tab. 1 – Boundary conditions used in the simulations

Variable	Wall Boundary conditions
α_D	Zero Gradient
ε	Zero Gradient
k	Zero Gradient
M_k	Zero Gradient
P	Zero Gradient
$\boldsymbol{u_D}, \boldsymbol{u_C}$	No Slip

Tab. 2 – Order of the numerical schemes used for the solution of the model equations

Term	Configuration
$\partial/\partial t$	1st order Euler explicit
$\nabla\psi$	Cell limited 2nd order
$\nabla \cdot (\boldsymbol{u_D}\alpha_D)$	2nd order with van Leer limiter
$\nabla \cdot (\boldsymbol{u_C}\alpha_C k)$	2nd order upwind

$\nabla \cdot (\boldsymbol{u_C} \alpha_C \varepsilon)$	2nd order upwind
$\nabla \cdot (\alpha \boldsymbol{u u})$	2nd order with Sweby limiter
$\nabla \cdot (\boldsymbol{u_D} M_k)$	1st order upwind
$\nabla^2 \psi$	2nd order
ψ_f	2nd order
$\nabla^{\perp} \psi$	Cell limited 2nd order

ψ is a generic variable, f denotes the face interpolation operator, $\nabla^{\perp}$ is the surface normal gradient.

The PBM was solved with the QMOM approach implemented in OpenFOAM as described by Buffo et al. (2016b, 2013). Six NDF moments were transported, resulting in three quadrature nodes and three weights.

The time-dependent solution of the CFD equations and the PBM was obtained through two different strategies, called weak coupling, already described by Gao et al. (2016), and offline coupling. With the first strategy, for each second of simulated time, the fluid dynamics equations coupled with the PBM are solved for 0.1s and then just the PBM is solved for the remaining 0.9s. With the offline coupling, on the other hand, the PBM is solved in a stationary frozen flow-field. The adoption of the Weak and the Offline Coupling strategies is acceptable since the disperse phase volume fraction is very low and since the mixing characteristic time, defined as the integral time scale of turbulence, is smaller than the breakage characteristic time scales (Buffo et al., 2016a).

The Weak and the Offline Coupling were both tested, starting the simulation with the disperse phase homogeneously distributed inside the volume as droplets of constant diameter equal to 700μm. The time evolution of the Sauter mean diameter, as obtained with the two coupling strategies, was compared to quantify the deviations between them. The maximum deviation of the Sauter mean diameter obtained with the Offline Coupling strategy is about 0.5% of the diameter as obtained with the Weak Coupling. The decoupling between continuous phase fluid dynamics and breakup phenomena is also confirmed by the experimental observations, as discussed in the following, since the dispersed droplets mainly follow the continuous flow field in the investigated operating condition. Given the enormous differences in term of computational time and the overall agreement between the two strategies, just the Offline Coupling was considered in the remaining part of this study.

5 Grid convergence study

Three different structured meshes were adopted to evaluate the grid convergence of the solution (Roache, 1998). The number of elements of the three meshes, named G1, G2 and G3, was 5.5×10^6, 2.2×10^6 and 0.60×10^6, respectively, resulting in a refinement ratio of 1.41, calculated on the spacing between the grid nodes of the impeller blades ($h_1 = 0.80$ mm for G1, $h_2 = 1.10$mm for G2 and $h_3 = 1.60$mm for G3).

A set of single-phase simulations with the three grids was performed and the grid convergence of the solution was evaluated considering axial and radial velocity profiles in different tank locations and turbulent variables profiles. Results confirm that mean flow variables reach grid independency with relatively coarse meshes, while much finer grids are required to obtain grid independent turbulent flow variables, as already found by Coroneo et al. (2011). In determining the properties of the dispersion, the correct prediction of the turbulent variables is of primary importance, since the breakage rate depends on the local turbulent dissipation rate (Li et al., 2017b).

For these reasons, the grid convergence study was performed on the predictions of the power number, $N_P = P_\varepsilon/\rho_C N^3 D^5$ of the RT at N equal to 500rpm, which experimental value is equal to 5. The impeller power consumption, P_ε, was calculated from the integral of the turbulent dissipation rate over the mass in the vessel. The values obtained with the three grids are 4.86 for G1, 4.60 for G2 and 3.71 for G3. The power numbers obtained with the three grids from the torque transferred from the moving walls are 5.09 for G1, 5.05 for G2 and 4.78 for G3. As reported in the literature (Coroneo et al., 2011), the power number obtained from the moment on the moving walls achieves grid independency with much coarser grids, similarly to the mean velocity field.

For the three grids, the grid convergence index (GCI) (Coleman and Stern, 1997) based on N_P obtained from the integral of the turbulent dissipation rate over the vessel mass is 2.79% for G1, 9.48% for G2 and 34.06% for G3, as can be seen in Fig. 1, this results in a

Richardson extrapolation (Roache, 1998) of N_P equal to 4.97, that is very close to the experimental value.

The total CPU time required on a octa-core Intel Xeon E5-1660 Dell Precision T5810 system operating under Linux for the single-phase flow calculation of the 9.8 L vessel under consideration is equal to 105, 38 and 3 hours for G1, G2 and G3, respectively. The spatial discretization and the related computational time requirements for the calculation of grid independent turbulent variables cannot be disregarded in the simulation of industrial size liquid-liquid stirred vessels, since the number of cells increases with the volume of the computational domain. The two-phase simulations were run on the CINECA HPC system MARCONI.

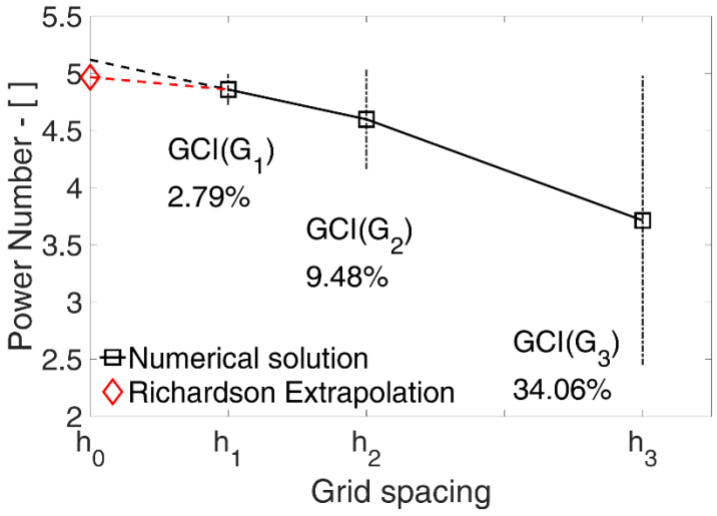

Fig. 1 – GCI (dashed lines) and Richardson extrapolation for the three grids considered.

6 Results

6.1Analysis of the continuous phase turbulent field

Being the turbulent variables paramount in the determination of the breakup frequency, the continuous phase turbulent velocity field was considered first, in order to evaluate the appropriateness of the selection of a single-phase turbulence model and to assess the turbulent dissipation rate predictions.

The continuous phase flow field was measured in single phase conditions (SP), with the stirred tank filled with water only, and in two-phase conditions (TP), with 0.1vol% of diesel fuel in water. Axial profiles of the mean and fluctuating velocity components of water measured in SP and TP conditions were analyzed. By means of example, fluctuating velocity axial profiles at different radial coordinates are shown in Fig. 2. The velocity components are divided by the impeller tip speed, $V_{tip} = \pi ND = 2.01$m/s, to make them dimensionless. In a preliminary investigation, three different replicates were collected with a diesel-fuel volume fraction of 5×10^{-4}, and a maximum standard deviation of $0.02V_{tip}$ was calculated. As can be observed in Fig. 2, the profiles at r/T = 0.22 perfectly overlap, whereas at r/T = 0.43 the water fluctuations in the presence of diesel fuel are slightly larger than the water fluctuations without droplets, especially in the region $0.44 < z/T < 0.56$, with a maximum deviation of $v'/V_{tip} = 0.017$ at z/T = 0.53. Unsurprisingly, since oil droplets closely follow fluctuations in the flow, 0.1% by volume of diesel fuel has a negligible effect on the mean flow field (Zhou and Kresta, 1998b).

Indeed, averaged velocity profiles of water with and without disperse phase almost perfectly overlap (not shown for brevity), and negligible differences are also visible for the water RMS velocity fluctuations with and without oil droplets. Having confirmed that under these operating conditions the presence of the disperse phase negligibly affects both the mean and the turbulent velocity field of the continuous phase, the single-phase k-ε model is an appropriate choice. The experimental determination of the turbulent dissipation rate was not performed in this work, since the validation of the turbulent flow field can be based on single-phase data collected in previous works from literature.

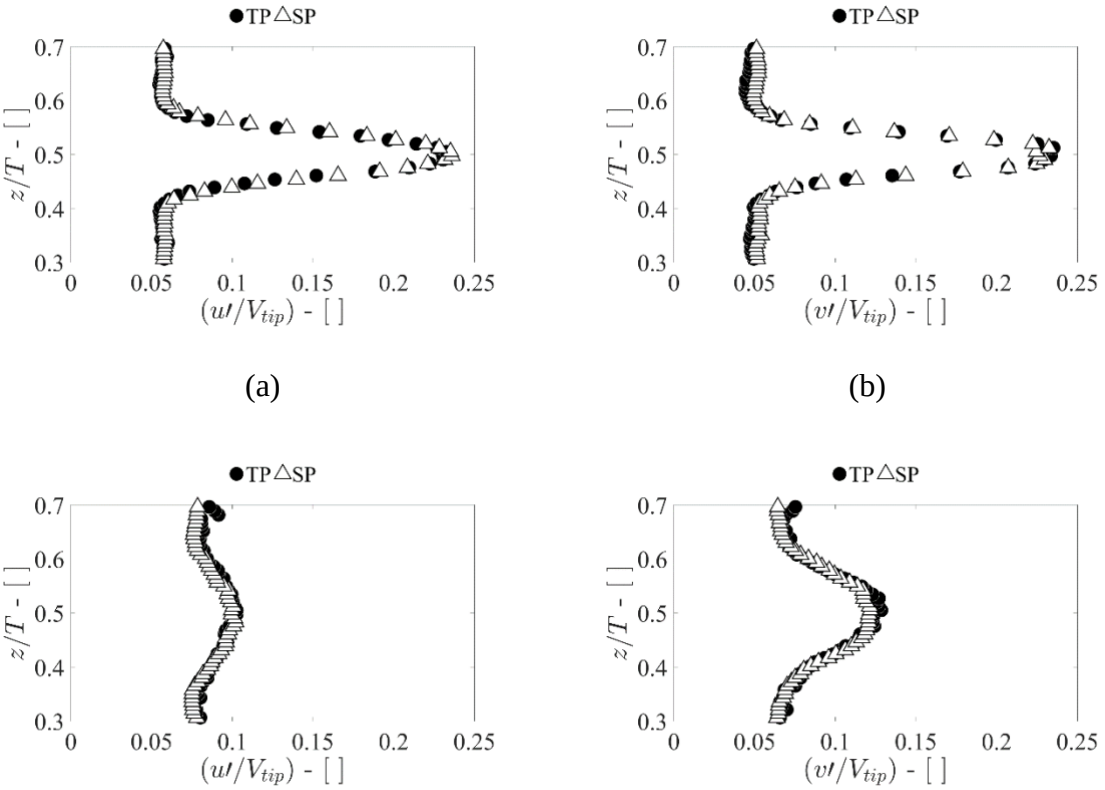

(a) (b)

(c) (d)

Fig. 2 – Axial profile of single-phase (SP) and two-phase (TP) axial (u') and radial (v') non-dimensional RMS of the water fluctuating velocities. Data are obtained on a plane midway two consecutive baffles at a dimensionless radial coordinate of r/T = 0.22 (a) and (b) and r/T = 0.43 (c) and (d).

6.2 Assessment of the turbulent kinetic energy dissipation rate predictions

The turbulent dissipation rate was not determined in this work since a very high spatial and time resolution would have been needed to collect the data (de Jong et al., 2009; Vejražka et al., 2018). In Fig.3, the radial profiles of non-dimensional turbulent dissipation rate at the impeller disk elevation obtained in this work with the G1 grid, that is the finer grid, are compared with results reported in previously published works with similar geometries. Additionally, in Fig.4 axial profiles of non-dimensional turbulent dissipation rate are compared with the experimental data obtained from turbulent kinetic energy balance by Escudié and Liné, (2003). In particular, Baldi et al. (2004) employed a direct method to obtain turbulent dissipation rate from measurements of the Reynolds stress gradients, performing LDA experiments as well; Escudié and Liné (2003) obtained the turbulent dissipation rate from a balance on the turbulent kinetic energy and from dimensional analysis. Sharp and Adrian (2001) employed a direct method to obtain turbulent dissipation rate from measurements, with different estimates methods (with

various assumptions of isotropy and axisymmetry) to obtain the unknown terms in the gradients of the Reynolds stress.

The comparison clearly shows that, although RANS simulations fail in reproducing the non-monotonic profile of the turbulent dissipation rate along the radial coordinate as already observed in previous works (Yeoh et al., 2004; Yoon et al., 2003), the predictions closely match the experimental data by Baldi et al. (2004) for r/T>0.22. Moreover, after *r/T* = 0.20 the slope of the ε profile is equal to that obtained by Yeoh et al. (2004) with LES simulations.

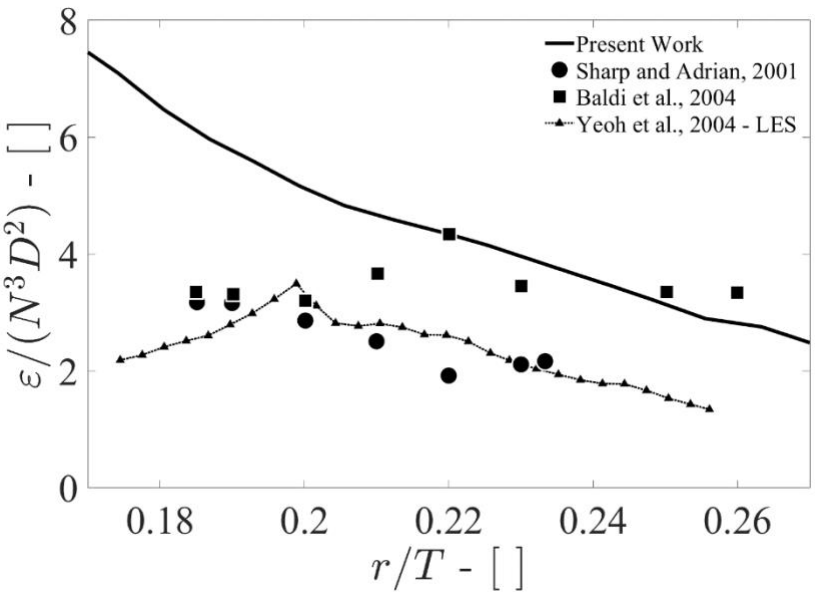

Fig. 3 – Comparison between numerical and experimental turbulent dissipation rate radial profiles from the literature and the present work results. Data are collected at an axial coordinate equal to the center of the impeller blade.

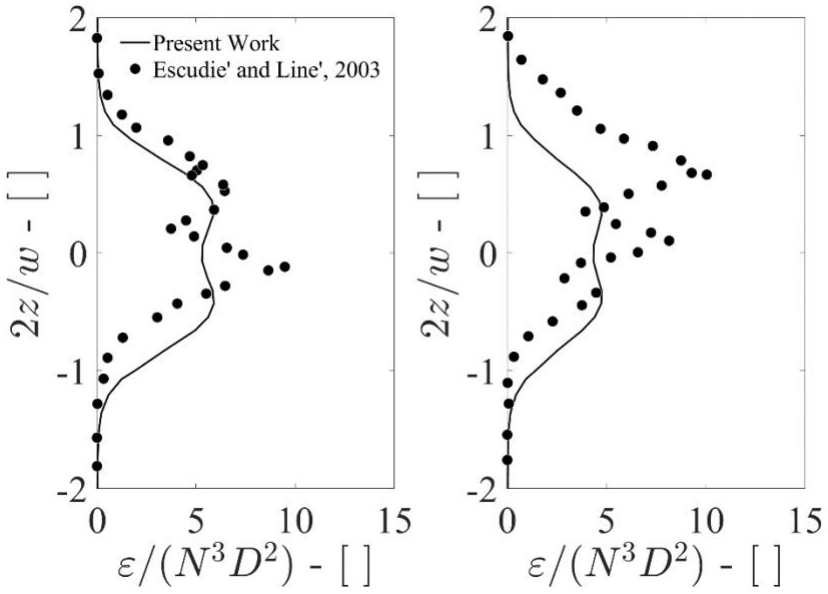

Fig. 4 – Non dimensional turbulent dissipation rate axial profiles obtained at a non dimensional radial coordinate of $r/T = 0.20$(a) and of $r/T = 0.22$(b).

Data in Fig. 4 are shown in terms of a scaled axial coordinate centered in the midpoint of the impeller blade height and divided by the blade height, w, equal to $0.2D$ = 0.0153m. The numerical results compare well with the experimental profile, with a closer agreement at r/T = 0.20 with respect to at r/T = 0.22, where the turbulent dissipation is underpredicted. It is worth recalling that these predictions are obtained without the use of adjustable parameters and that a slight difference in blade and disk thickness can affect both mean flow and turbulent distributions, thus geometrical differences could explain the profile

discrepancies. Moreover, it is well known that the organized periodic flow structures generated by the impeller rotation affect the turbulent kinetic energy (and its dissipation) up to a non-dimensional radial coordinate (r/T) of 0.225 and this flow feature cannot be predicted by the RANS multiple reference frame modelling framework adopted in this study.

Being the turbulent dissipation rate responsible for the droplet breakage, in Tab. 3 the maximum value of the turbulence dissipation rate obtained with the simulations with the G1 grid excluding the zone at $r/T<1/6$ is compared with the experimental data by Escudié and Liné, (2003), Baldi and Yianneskis, (2004), Ducci and Yianneskis, (2005) and with the RANS simulations of Delafosse et al. (2008), as already done by the latter author. The analysis excludes the radial location of the impeller ($r/T<1/6$) that usually cannot be investigated with optical techniques, since the laser light is blocked by the impeller blade passage. For $r/T>1/6$ a maximum value of 10.2 is found in the simulations, that is in fair agreement with the results from the literature.

For $r/T<1/6$, at the non-dimensional coordinate of $r/T = 0.08$ the maximum predicted non-dimensional turbulent dissipation rate is that is equal to 84.

Tab. 3 – Maximum energy dissipation rate and its position as obtained from experimental and numerical works from the literature and the present work.

	Escudié and Liné, (2003)	Baldi and Yianneskis, (2004)	Ducci and Yianneskis, (2005)	Delafosse et al. (2008)	**Present work**
$\frac{\varepsilon_{max}}{N^3D^2}$	14	10.5	9.4	11	10.2
r/T	0.22	0.224	0.225	0.16	0.17

Overall, the evaluation of the local predicted values of ε in the impeller region leads to conclude that notwithstanding the known approximation of RANS-based modelling, a fair representation of the turbulent dissipation rate can be achieved minimizing the numerical approximations, thus providing a reliable basis for the droplet size distribution calculation.

6.3Discussion

A map of the turbulent dissipation rate obtained with the G1 and G3 grids is shown in Fig. 5 on a vertical plane midway two consecutive baffles. As expected, the spatial distribution of turbulent dissipation rate is remarkably inhomogeneous, the highest values are limited in the proximity of the impeller and large differences are found with the two grids.

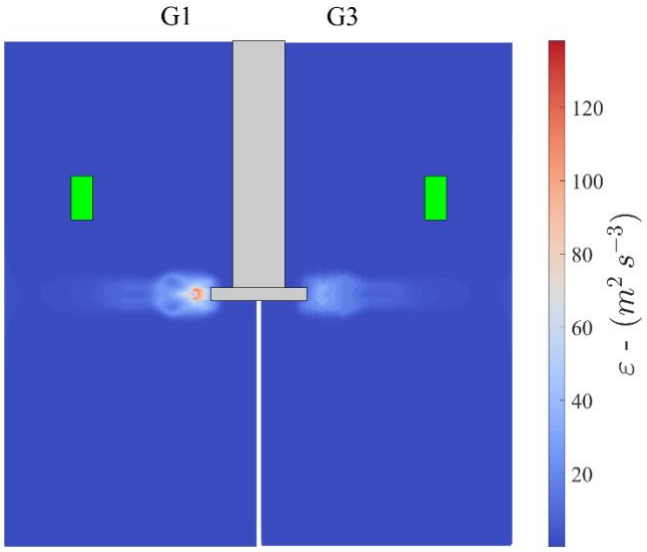

Fig. 5 – Comparison between the turbulent dissipation rate field generated with the G1 grid (left) and the G3 grid (right) on a vertical plane midway two consecutive baffles. In green, the section corresponding to the sampling zone.

Focusing the analysis of the predicted ε in the sampling zone adopted for the experimental DSD determination, that is depicted in green in Fig. 5, the ratio of the average turbulent dissipation rate as predicted by the two grids is:

$$\varepsilon(G1)\Big/_{\varepsilon(G3)} \approx {}^{0.077}\Big/_{0.065} = 1.20 \tag{14}$$

which is very close to the ratio of the power numbers obtained from P_ε:

$$N_P(G1)\Big/_{N_P(G3)} \approx {}^{4.86}\Big/_{3.71} = 1.31 \tag{15}$$

This result confirms that correcting the turbulent dissipation rate inside the breakage kernels with the ratio of the power number obtained from the simulation and the

experimental power number may be a workable approach to avoid long computational times (Gao et al., 2016).

The spatial distribution of ε has a significant impact on the breakup phenomena, as can be observed in Fig. 6 on a vertical plane between two consecutive baffles. The droplet breakup frequency is obtained with G1 right after the fluid dynamics solution converged.

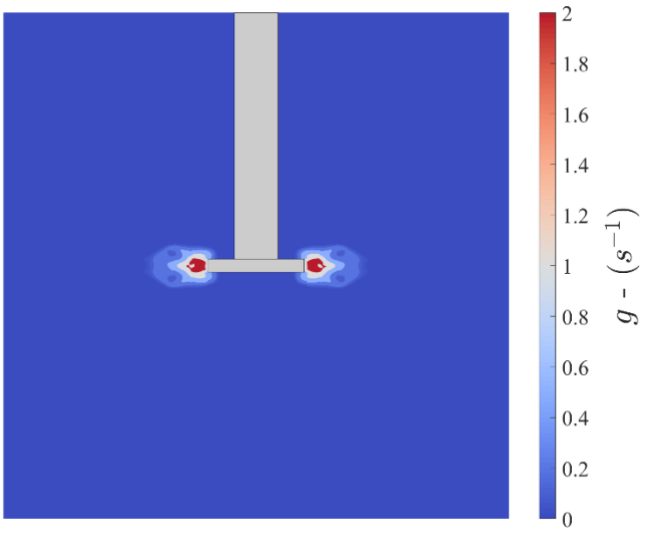

Fig. 6 – Breakup frequency on a vertical plane midway two consecutive baffles obtained with G1.

As can be observed, the breakup frequency is significant just where ε is high. Since for this system the breaking events are meaningful just in the proximity of the impeller, as shown in Fig. 6, the correcting factor should be derived from the ratio of the ε volume average obtained either in a region close the impeller or as the ratio of the maximum ε in

the system. In fact, the breakup rate in the bulk of the tank is four orders of magnitude smaller than in the impeller region.

In those scenarios the correcting factors for our system would be:

$$\varepsilon_{impeller}(G1)\Big/\varepsilon_{impeller}(G3) \approx {}^{24.30}\Big/_{15.16} = 1.60 \quad (16)$$

$$\varepsilon_{max}(G1)\Big/\varepsilon_{max}(G3) \approx {}^{291.6}\Big/_{85.2} = 3.42 \quad (17)$$

As known, the grid has a non-linear effect on the turbulent dissipation rate and with G3 it is underestimated by 16% in the bulk, by 38% around the impeller ($\varepsilon_{impeller}$) and by 71% of the peak maximum value (ε_{max}), with respect to G1. This observation confirms that in case of underprediction of the turbulent dissipation rate, as can be the case of relatively coarse discretization of large volumes, a correction for the breakage kernels based on ε values in the impeller region instead of on the overall power dissipation is more appropriate.

The spatial distribution of the breakage frequency in a stirred tank was already numerically studied by Vonka and Soos, (2015) who stated that a small zone located in the proximity of the impeller may have a significant effect on the DSD. In their analysis they used a 316,803 elements mesh in a tank of diameter equal to 150 mm and found a $\varepsilon_{max}/\langle\varepsilon\rangle$ value of 290 (with $\langle\varepsilon\rangle$ being the volume average of the turbulent dissipation rate) obtained

with a $k-\varepsilon$ model with the physical properties of the mixture, that compared well with the value of $\varepsilon_{max}/\langle\varepsilon\rangle = 550$ obtained for a similar system in a previous work with a LES simulation and a 1.6 million elements mesh (Soos et al., 2013).

The value of $\varepsilon_{max}/\langle\varepsilon\rangle = 550$ agrees with our value of $\varepsilon_{max}/\langle\varepsilon\rangle = 387$ obtained with G1 (the grid with 5,500,000 elements). However, Soos et al. (2013) reported that the power number calculated as the integral of the turbulent dissipation rate on the whole tank volume was underpredicted with respect to the values in the literature, pointing to the fact that the turbulent field may, in fact, have been underpredicted (even with a 1.6 million elements mesh in a tank of diameter equal to 150 mm).

In principle, high order turbulence phenomena such as intermittency may have an effect in the description of the drop breakage in agitated systems, but these phenomena mostly affect the breakup dynamics. Minor differences are expected on the prediction of the DSD at the steady state (Gao et al., 2016; Li et al., 2017a).

6.4Analysis of size distribution and velocity of the droplets

The experimental DSD obtained as described in Section 2 from triplicate measurements at *N* = 500 rpm are shown Fig. 7, where the distribution probability is expressed in terms of volume fraction with respect to the total disperse phase volume in the sample.

The experimental measurements of the DSD show good reproducibility, as shown by the error bars which values are the standard deviations for each diameter category, that

range from 1.4×10^{-4} to 3.8×10^{-3}. The corresponding coefficients of variations for each diameter category range from 0.8% to 23.4% for the droplets with average diameters equal to 8.00×10^{-5} m and to 1.47×10^{-4} m respectively.

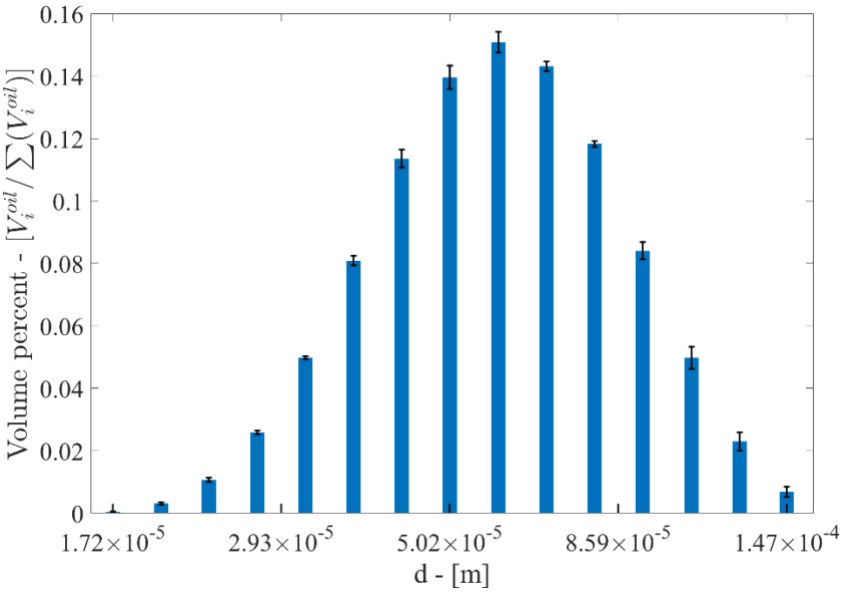

Fig. 7 – Experimental DSD obtained from triplicate measurements at N = 500rpm and error bars representing standard deviations

The experiments confirm that the size of the droplets is of the order of tens of micrometers and that the DSD is relatively narrow. The experimental DSD is then used to validate the numerical results obtained with the modelling procedure described in Section 3.

Since the experiments provided the DSD in the sample, a method to reconstruct the NDF in the postprocessing calculations was used, being this information not promptly

available with the QMOM. The EQMOM with a gamma distribution as a kernel density function was used, in the postprocessing stage, to obtain the continuous DSD from the moment set available from the calculation (Marchisio and Fox, 2013). The results obtained with the coarsest mesh G3 are shown in Fig. 8.

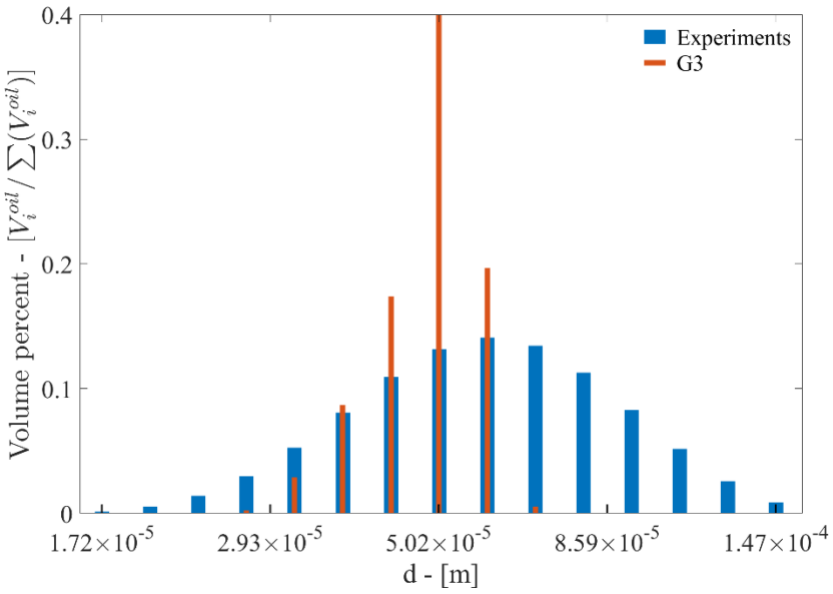

Fig. 8 – Comparison between experimental and numerical DSD as obtained with the G3 grid.

As already mentioned, the numerical DSD is obtained through an average over the cells in the sampling position described in Section 2. The reconstructed DSD obtained from the simulation, with the two calculated quadrature nodes equal to 36.3μm and 49.6μm, was discretized in the same diameter bins used in the experimental DSD, for an easier comparison. The DSD is expressed in terms of volume fraction, to match the experimental data. Almost no differences were observed in the DSD reconstructed from the moments

collected in different tank zones. This result confirms that the DSD is homogeneous throughout the tank and consequently the choice of the sampling point is not pivotal.

Despite an underestimation of the power consumed by the impeller, P_ε, the DSD from the simulation is in acceptable agreement with the experimental one. A numerical Sauter mean diameter of 47.9μm was obtained whereas the experimentally measured diameter was equal to 47.6μm. In addition to the Sauter mean diameter, the Spraytec laser diffraction system measures the ratio between the fourth and the third NDF moment, also called the De Brouckere mean diameter, that is equal to 61.7μm. The numerical De Brouckere mean diameter as obtained with G3 is equal to 49.0μm.

The DSD as obtained with the simulation with the finest grid G1 was calculated as well, with the same procedure described above for G3, and it is shown in Fig. 9. The two calculated quadrature nodes are equal to 23.8μm and 32.4μm. As expected, in this case a lower Sauter mean diameter of 31.7μm was obtained in the sampling volume since the turbulent dissipation rate is higher, as shown in Section 5. The numerical De Brouckere mean diameter as obtained with G1 is equal to 32.0μm.

These results confirm the importance of the computational grids on the prediction of the turbulent variables and their subsequent effects on the resulting DSD.

Having found that an underestimation of the turbulent dissipation rate by the coarser grid leads to a better agreement with the experiments entails that the set of parameters used in the breakage kernel is grid dependent (i.e. dependent on the coarse multiblock grid

adopted by Alopaeus et al. (2002) for the fitting procedure) and it is not suitable for very fine grids.

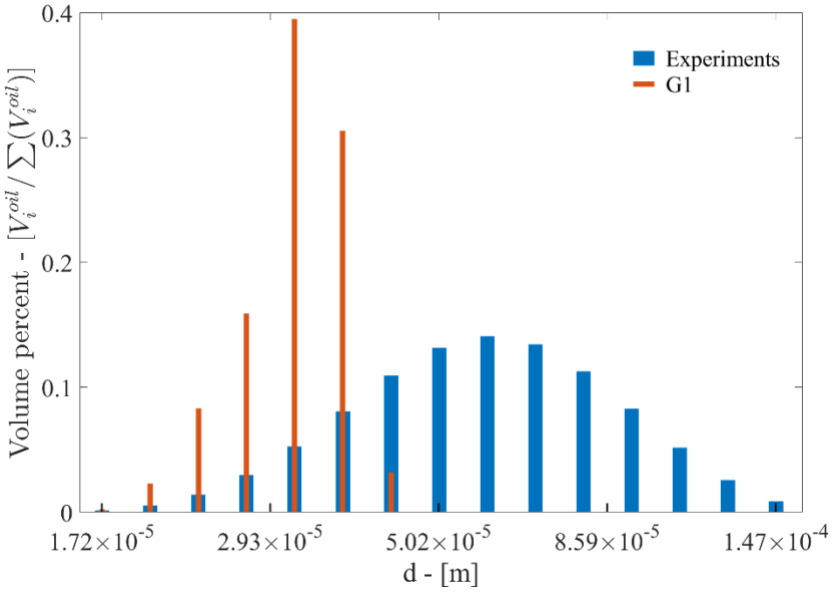

Fig. 9 - Comparison between experimental and numerical DSD as obtained with the G1 grid.

~~Although the variability of the turbulent dissipation rate predictions can be compensated with an adjustment of the set of parameters of the breakage kernel, the selection of their values results in a loss of fully predictive capabilities of the simulations.~~

Although the variability of the turbulent dissipation rate predictions could be compensated with an adjustment of the set of parameters of the breakage kernel, this approach would require large amounts of experiments in order to fit the parameters to flow conditions and system properties data. Moreover, the setting of these values based on empirical approach will result in a loss of fully predictive capabilities of the simulations.

In addition to the droplets size distribution, the oil droplets averaged flow field was measured, and negligible differences were found with respect to the water averaged flow field. In fact, the droplet and the seeding particles relaxation times are very similar, due to the droplet small size. The axial profiles collected at different axial coordinates of dimensionless axial and radial mean velocity are shown in Fig. 10, together with dimensionless axial and radial mean velocity profiles obtained from the simulation with G1.

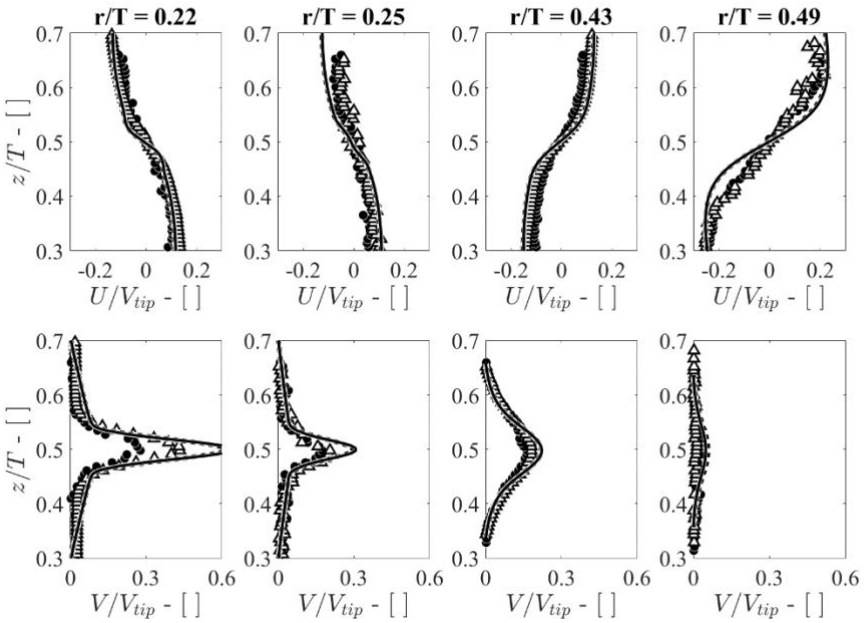

Fig. 10 - Axial profile of axial (top) and radial (bottom) non-dimensional mean velocities of oil (black circles) and water (white triangles)as obtained from the experiments and of oil (solid line) and water (dashed line) from the numerical simulation with G1. Data are obtained on a plane midway two consecutive baffles at different dimensionless radial coordinates.

Fig. 10 shows that diesel fuel and water dimensionless averaged velocity profiles obtained from the experiments almost perfectly overlap, confirming that the slip velocity between the two-phases is negligibly small. The maximum standard deviation obtained from triplicate measurements is $0.06V_{tip}$ for the diesel fuel and $0.03V_{tip}$ for the water, and the average standard deviation for the diesel fuel is $0.013V_{tip}$, while for the water it is $0.007V_{tip}$. Numerical and experimental results are in acceptable agreement, with just some differences in the profile shape and in the maximum radial velocity, due to differences in the spatial resolution of experiments and CFD. The maximum deviation registered is found between the diesel fuel experimental and numerical radial velocities at r/T = 0.22, with a value of $0.27V_{tip}$ while the average deviation is $0.0077V_{tip}$.

Numerical diesel fuel and water dimensionless averaged velocity profiles as predicted by G1 perfectly overlap, reproducing the experimental findings.

7 Scalar correction

The strong dependency of the turbulent variables prediction on the grid size and today's practical impossibility to reach grid independency on turbulent variables in industrial scale equipment drive the need to find a method to obtain reliable DSD prediction with any grid size. Gao et al. (2016) proposed a correction on the turbulent dissipation rate based on the ratio between the experimental power number and the power number as

obtained from the integral of the turbulent dissipation rate on the whole volume. Following the discussion of Section 6.3, a refined correction is proposed, based on the maximum ε, rather than on the average over the whole volume. In fact, as already mentioned, the breakup rate in the bulk is four orders of magnitude smaller than the maximum breakup rate found in the tank. On the other hand, the average breakup rate in the volume swept by the impeller blades is approximately 30% of the maximum breakup rate. Having a non-negligible breakup rate in the impeller region, $\varepsilon_{impeller}$ was used to derive the proposed scalar correction.

Two different aspects have been addressed in deriving the correction, the former being the derivation of a set of grid independent breakup kernel parameters and the latter being the identification of a grid dependent scalar correction factor.

The first step to derive the grid independent breakup kernel parameters requires to evaluate $\varepsilon_{impeller}$ from the three grids G1, G2 and G3 and then calculate the Richardson extrapolation (Roache, 1998), as shown in Fig. 11.

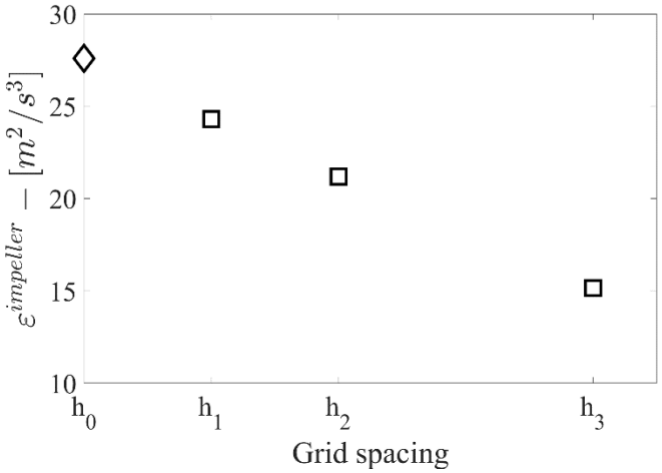

Fig. 11 – Average turbulent dissipation rate in the volume swept by the impeller blades as predicted by the three grids (squares) and Richardson extrapolation (diamond).

The Richardson extrapolation allows to obtain a presumed value at zero grid spacing (*infinitely fine mesh*) from values obtained at higher grid spacing. Exploiting this estimate and the fact that the turbulent dissipation rate from G3 predicts a DSD that is in better agreement with the experimental data (Fig. 8) a set of breakup kernel parameters for an infinitely fine mesh, C_1^0, C_2^0, C_3^0, was then calculated. In fact, as already pointed out in Section 6.4, the three parameters of the breakup kernel are not grid independent. Thus, the breakup kernel parameters for an infinitely fine mesh are obtained as:

$$C_1^0 = C_1 \left(\varepsilon_{impeller}^{G3} \Big/ \varepsilon_{impeller}^{RE} \right)^{1/3} = 3.68 \left(15.16 \Big/ 28.55 \right)^{1/3} = 2.98 \qquad (18)$$

$$C_2^0 = C_2 \left(\varepsilon_{impeller}^{G3} \Big/ \varepsilon_{impeller}^{RE} \right)^{-2/3} = 0.0775 \left(15.16 \Big/ 28.55 \right)^{-2/3} = 0.12 \qquad (19)$$

$$C_3^0 = C_3\left(\varepsilon_{impeller}^{G3}\Big/\varepsilon_{impeller}^{RE}\right)^{-1/3} = 0.2\left(15.16/28.55\right)^{-1/3} = 0.25 \qquad (20)$$

Where $\varepsilon_{impeller}^{G3}$ and $\varepsilon_{impeller}^{RE}$ are the $\varepsilon_{impeller}$ as obtained with G3 and from the Richardson extrapolation respectively. The exponents of the terms between brackets are derived from the functional form of the breakup kernel in Eq. (10). The underlying hypothesis for the derivation of C_1^0, C_2^0, C_3^0 is that using C_1, C_2, C_3 reliable results are produced when the simulation predicts an average turbulent dissipation rate in the volume swept by the impeller blades equal to $\varepsilon_{impeller}^{G3}$.

Having derived a set of potentially grid independent parameters, a grid dependent scalar correction, F_{Gi}, for the turbulent dissipation rate in the kernel is suggested when large vessel volumes, computational limitations or time constrains do not allow a grid independent solution. For a simulation performed with a generic grid G_i, giving a value of turbulent dissipation rate in the volume swept by the impeller blades equal to $\varepsilon_{impeller}^{Gi}$, the correction can be obtained as:

$$F_{Gi} = \varepsilon_{impeller}^{RE} \,/\varepsilon_{impeller}^{Gi} \qquad (21)$$

It is worth observing that for different impeller types, the $\varepsilon_{impeller}^{RE}$ can be obtained from preliminary small scale simulations at equal Reynolds number, thus limiting the computational cost.

As a result, the following modified form of Eq. (11) can be adopted:

$$g = C_1^0\ (\varepsilon_{Gi}F_i)^{1/3} erfc\left(\sqrt{\frac{C_2^0\sigma}{\rho_C(\varepsilon_{Gi}F_i)^{2/3}{d_D}^{5/3}} + \frac{C_3^0\mu_D}{\sqrt{\rho_C\rho_D}(\varepsilon_{Gi}F_i)^{1/3}{d_D}^{4/3}}}\right) \qquad (22)$$

With ε_{Gi} being the local turbulent dissipation rate obtained with the grid Gi and C_1^0, C_2^0 and C_3^0 are the grid independent kernel parameters.

The correction method proposed might be particularly useful for the simulation of large-scale equipment, where ensuring grid independent solution would require unaffordable long computational times.

8 Conclusions

In this work, RANS TFM simulations coupled with a PBM for the determination of the DSD of diesel fuel in water in a mechanically stirred tank were run in OpenFOAM. The PBM was solved in the simplified case of negligible coalescence events with QMOM and the resulting DSDs were compared to experimental data collected from *ad hoc* experiments.

Focusing on a single operating condition allowed to thoroughly investigate the effect of the turbulent variables on the breakage phenomena and on the resulting DSD, in the context of the RANS CFD-PBM simulations.

The turbulent flow field predicted by the simulations was systematically validated with numerical data from the literature and with original and published experimental measurements, finding an acceptable agreement.

Different computational grids were tested, to explore the effects of the prediction of the turbulent variables on the numerical results. The adoption of a fine grid that satisfactorily predicted the turbulent flow field resulted in a larger underprediction of the DSD, with respect to a coarser grid, meaning that the parameters in the breakup kernel are grid dependent and they are not suitable for very fine grids.

In the discussion section, the turbulent dissipation rate field and the resulting breakage phenomena were analyzed, confirming that the turbulent dissipation rate and the breakup frequency are order of magnitude higher in the proximity of the impeller than in the bulk and that the volume swept by the impeller is responsible for almost the totality of the breakup events.

A way to deal with the grid dependency is hypothesized, calculating a set of grid independent breakup kernel parameters and adopting the scalar correction for the turbulent dissipation rate in the breakup kernel proposed by Gao et al. (2016), deriving it from local quantities rather than volume averaged ones.

9 Acknowledgments

We acknowledge the CINECA award under the ISCRA initiative, for the availability of high performance computing resources and support.

The collaboration of Professor Alberto Arcioni in determining some of the physical properties of the mixture and of Rodolfo Lucchi in carrying out part of the experimental program are gratefully acknowledged.

A. Paglianti acknowledges the support of the Italian Government through the Grant "Excellent Departments" 2018-2022.

10 Nomenclature

C	Off-bottom clearance
C_1, C_2, C_3	Alopaeus breakage kernel parameters
C_1^0,C_2^0, C_3^0	Alopaeus breakage kernel parameters for an infinitely fine mesh
$C_{1\varepsilon}$, $C_{2\varepsilon}$, C_μ	$k-\varepsilon$ turbulence model parameters
C_D	Drag coefficient
d_D	Drop diameter
d_i	Nodes of quadrature
D	Impeller diameter
$\boldsymbol{E}$	Rate of deformation
$\boldsymbol{F}$	Interphase momentum transfer term
$\boldsymbol{F}_{drag,CD}$	Interphase drag force
F_{Gi}	Grid dependent scalar correction for the grid Gi
$\boldsymbol{g}$	Gravity vector
g	Breakup frequency
$G1$, $G2$, $G3$	Finest, intermediate, and coarsest grid used for the simulations
h_1, h_2, h_3	G1, G2 and G3 spacing of the nodes on the impeller blade
H_L	Liquid height
H_T	Tank height
k	Turbulent kinetic energy
M_k	Reduced NDF moment of order k
n	Number density function
N	Impeller rotational speed
N_p	Power number
N_q	Order of approximation of the NDF
P	Pressure

P_ε	Impeller power consumption from the volume integral of ε
r	Radial coordinate
Re	Reynolds number
Re_p	Particle Reynolds number
t	Time
T	Tank diameter
$\boldsymbol{u_C}$	Continuous phase velocity vector
$\boldsymbol{u_D}$	Dispersed phase velocity vector
u'_{RMS}	Continuous phase RMS of the fluctuating axial velocity
U	Continuous phase average axial velocity
V_{tip}	Impeller tip speed
v'	Continuous phase RMS of the fluctuating radial velocity
V	Continuous phase average radial velocity
V_i^{oil}	Diesel fuel volume fraction of the i-th diameter bin
w	Impeller blade height
w_i	Weights of quadrature
z	Axial coordinate

Greek letters

α_C	Continuous phase volume fraction
α_D	Dispersed phase volume fraction
β	Daughter distribution function
ε	Turbulent dissipation rate
$\langle\varepsilon\rangle$	Volume averaged turbulent dissipation rate
ε_{Gi}	Local ε as obtained with the Gi grid
$\varepsilon_{impeller}$	Average ε in the volume swept by the impeller
$\varepsilon_{impeller}^{Gi}$	$\varepsilon_{impeller}$ as obtained with the Gi grid

$\varepsilon_{impeller}^{RE}$	Richardson extrapolation of $\varepsilon_{impeller}$
ε_{max}	Maximum ε in the system
λ	Wavelength
μ_C	Continuous phase dynamic viscosity
μ_D	Dispersed phase dynamic viscosity
μ_t	Turbulent viscosity
ρ_C	Continuous phase density
ρ_D	Dispersed phase density
σ	Interfacial tension
σ_k, σ_ε	$k-\varepsilon$ turbulence model parameters
$\boldsymbol{\tau_D}$	Dispersed phase viscous stress tensor
$\boldsymbol{\tau^t}$	Reynolds stress tensor
ψ	Generic variable

11 References

Afshar Ghotli, R., Raman, A.A.A., Ibrahim, S., Baroutian, S., 2013. LIQUID-LIQUID MIXING IN STIRRED VESSELS: A REVIEW. Chem. Eng. Commun. 200, 595–627. https://doi.org/10.1080/00986445.2012.717313

Alopaeus, V., Koskinen, J., I. Keskinen, K., Majander, J., 2002. Simulation of the population balances for liquid–liquid systems in a nonideal stirred tank. Part 2—parameter fitting and the use of the multiblock model for dense dispersions. Chem. Eng. Sci. 57, 1815–1825. https://doi.org/10.1016/S0009-2509(02)00067-2

Alopaeus, V., Koskinen, J., Keskinen, K.I., 1999. Simulation of the population balances for liquid–liquid systems in a nonideal stirred tank. Part 1 Description and qualitative validation of the model. Chem. Eng. Sci. 54, 5887–5899. https://doi.org/10.1016/S0009-2509(99)00170-0

Amani, A., Balcázar, N., Castro, J., Oliva, A., 2019. Numerical study of droplet deformation in shear flow using a conservative level-set method. Chem. Eng. Sci. 207, 153–171. https://doi.org/10.1016/j.ces.2019.06.014

Azizi, F., Taweel, A.M. Al, 2011. Turbulently flowing liquid–liquid dispersions. Part I: Drop breakage and coalescence. Chem. Eng. J. 166, 715–725. https://doi.org/10.1016/j.cej.2010.11.050

Bakker, A., Haidari, A.H., Oshinowo, L.M., 2001. Realize greater benefits from CFD. Chem. Eng. Prog. 97, 45–53.

Baldi, S., Ducci, A., Yianneskis, M., 2004. Determination of Dissipation Rate in Stirred Vessels

Through Direct Measurement of Fluctuating Velocity Gradients. Chem. Eng. Technol. 27, 275–281. https://doi.org/10.1002/ceat.200401979

Baldi, S., Yianneskis, M., 2004. On the quantification of energy dissipation in the impeller stream of a stirred vessel from fluctuating velocity gradient measurements. Chem. Eng. Sci. 59, 2659–2671. https://doi.org/10.1016/j.ces.2004.03.021

Baldyga, J., Podgórska, W., 1998. Drop break-up in intermittent turbulence: maximum stable and transient sizes of drops. Can. J. Chem. Eng. 76, 456–470. https://doi.org/10.1002/cjce.5450760316

Boccardo, G., Sethi, R., Marchisio, D.L., 2019. Fine and ultrafine particle deposition in packed-bed catalytic reactors. Chem. Eng. Sci. 198, 290–304. https://doi.org/10.1016/j.ces.2018.09.024

Bourne, J.R., Yu, S., 1994. Investigation of micromixing in stirred tank reactors using parallel reactions. Ind. Eng. Chem. Res. 33, 41–55. https://doi.org/10.1021/ie00025a007

Buffo, A., De Bona, J., Vanni, M., Marchisio, D.L., 2016a. Simplified volume-averaged models for liquid–liquid dispersions: Correct derivation and comparison with other approaches. Chem. Eng. Sci. 153, 382–393. https://doi.org/10.1016/j.ces.2016.07.032

Buffo, A., Marchisio, D.L., 2014. Modeling and simulation of turbulent polydisperse gas-liquid systems via the generalized population balance equation. Rev. Chem. Eng. 30, 73–126. https://doi.org/10.1515/revce-2013-0015

Buffo, A., Marchisio, D.L., Vanni, M., Renze, P., 2013. Simulation of polydisperse multiphase systems using population balances and example application to bubbly flows. Chem. Eng. Res. Des. 91, 1859–1875. https://doi.org/10.1016/j.cherd.2013.06.021

Buffo, A., Vanni, M., Marchisio, D.L., 2016b. On the implementation of moment transport equations in OpenFOAM: Boundedness and realizability. Int. J. Multiph. Flow 85, 223–235. https://doi.org/10.1016/j.ijmultiphaseflow.2016.06.017

Buffo, A., Vanni, M., Marchisio, D.L., 2012. Multidimensional population balance model for the simulation of turbulent gas–liquid systems in stirred tank reactors. Chem. Eng. Sci. 70, 31–44. https://doi.org/10.1016/j.ces.2011.04.042

Castellano, S., Carrillo, L., Sheibat-Othman, N., Marchisio, D., Buffo, A., Charton, S., 2019. Using the full turbulence spectrum for describing droplet coalescence and breakage in industrial liquid-liquid systems: Experiments and modeling. Chem. Eng. J. 374, 1420–1432. https://doi.org/10.1016/j.cej.2019.06.032

Coleman, H.W., Stern, F., 1997. Uncertainties and CFD Code Validation. J. Fluids Eng. 119, 795. https://doi.org/10.1115/1.2819500

Coroneo, M., Montante, G., Paglianti, A., Magelli, F., 2011. CFD prediction of fluid flow and mixing in stirred tanks: Numerical issues about the RANS simulations. Comput. Chem. Eng. 35, 1959–1968. https://doi.org/10.1016/j.compchemeng.2010.12.007

Coulaloglou, C.A., Tavlarides, L.L., 1977. Description of interaction processes in agitated liquid-liquid dispersions. Chem. Eng. Sci. 32, 1289–1297. https://doi.org/10.1016/0009-2509(77)85023-9

de Jong, J., Cao, L., Woodward, S.H., Salazar, J.P.L.C., Collins, L.R., Meng, H., 2009. Dissipation rate estimation from PIV in zero-mean isotropic turbulence. Exp. Fluids 46, 499–515. https://doi.org/10.1007/s00348-008-0576-3

Delafosse, A., Line, A., Morchain, J., Guiraud, P., 2008. LES and URANS simulations of hydrodynamics in mixing tank: Comparison to PIV experiments. Chem. Eng. Res. Des. 86, 1322–1330. https://doi.org/10.1016/j.cherd.2008.07.008

Derksen, J.J., Van Den Akker, H.E.A., 2007. Multi-Scale Simulations of Stirred Liquid–Liquid Dispersions. Chem. Eng. Res. Des. 85, 697–702. https://doi.org/10.1205/cherd06161

Di Miceli Raimondi, N., Prat, L., Gourdon, C., Cognet, P., 2008. Direct numerical simulations of mass transfer in square microchannels for liquid–liquid slug flow. Chem. Eng. Sci. 63, 5522–5530. https://doi.org/10.1016/j.ces.2008.07.025

Drumm, C., Attarakih, M.M., Bart, H.-J., 2009. Coupling of CFD with DPBM for an RDC extractor. Chem. Eng. Sci. 64, 721–732. https://doi.org/10.1016/j.ces.2008.05.041

Ducci, A., Yianneskis, M., 2005. Direct determination of energy dissipation in stirred vessels with two-point LDA. AIChE J. 51, 2133–2149. https://doi.org/10.1002/aic.10468

Escudié, R., Liné, A., 2003. Experimental analysis of hydrodynamics in a radially agitated tank. AIChE J. 49, 585–603. https://doi.org/10.1002/aic.690490306

Falzone, S., Buffo, A., Vanni, M., Marchisio, D.L., 2018. Simulation of Turbulent Coalescence and Breakage of Bubbles and Droplets in the Presence of Surfactants, Salts, and Contaminants, in: Advances in Chemical Engineering. Academic Press Inc., pp. 125–188. https://doi.org/10.1016/bs.ache.2018.01.002

Gao, Z., Li, D., Buffo, A., Podgórska, W., Marchisio, D.L., 2016. Simulation of droplet breakage in turbulent liquid–liquid dispersions with CFD-PBM: Comparison of breakage kernels. Chem. Eng. Sci. 142, 277–288. https://doi.org/10.1016/j.ces.2015.11.040

Hu, X., Passalacqua, A., Fox, R.O., 2015. Application of quadrature-based uncertainty quantification to the NETL small-scale challenge problem SSCP-I. Powder Technol. 272, 100–112. https://doi.org/10.1016/j.powtec.2014.11.030

Jaworski, Z., Pianko-Oprych, P., 2002. Two-Phase Laminar Flow Simulations in a Kenics Static Mixer. Chem. Eng. Res. Des. 80, 910–916. https://doi.org/10.1205/026387602321143462

Jaworski, Z., Pianko-Oprych, P., Marchisio, D.L., Nienow, A.W., 2007. CFD Modelling of Turbulent Drop Breakage in a Kenics Static Mixer and Comparison with Experimental Data. Chem. Eng. Res. Des. 85, 753–759. https://doi.org/10.1205/cherd06179

Kálal, Z., Jahoda, M., Fořt, I., 2014. Modelling of the Bubble Size Distribution in an Aerated Stirred Tank: Theoretical and Numerical Comparison of Different Breakup Models. Chem. Process Eng. 35, 331–348. https://doi.org/10.2478/cpe-2014-0025

Karimi, M., Andersson, R., 2020. Stochastic simulation of droplet breakup in turbulence. Chem. Eng. J. 380, 122502. https://doi.org/10.1016/j.cej.2019.122502

Khajeh Naeeni, S., Pakzad, L., 2019. Experimental and numerical investigation on mixing of dilute oil in water dispersions in a stirred tank. Chem. Eng. Res. Des. 147, 493–509. https://doi.org/10.1016/j.cherd.2019.05.024

Laakkonen, M., Alopaeus, V., Aittamaa, J., 2006. Validation of bubble breakage, coalescence and mass transfer models for gas–liquid dispersion in agitated vessel. Chem. Eng. Sci. 61, 218–228. https://doi.org/10.1016/j.ces.2004.11.066

Laurenzi, F., Coroneo, M., Montante, G., Paglianti, A., Magelli, F., 2009. Experimental and computational analysis of immiscible liquid–liquid dispersions in stirred vessels. Chem. Eng.

Res. Des. 87, 507–514. https://doi.org/10.1016/j.cherd.2008.12.007

Leng, D.E., Calabrese, R. V., 2016. Immiscible Liquid-Liquid Systems, in: Kresta, S.M., Etchells, A.W.I., Dickey, D.S., Atiemo-Obeng, V.A. (Eds.), Advances in Industrial Mixing: A Companion to the Handbook of Industrial Mixing. Wiley & Sons, Inc., Hoboken, New Jersey, pp. 457–463.

Li, D., Buffo, A., Podgórska, W., Marchisio, D.L., Gao, Z., 2017a. Investigation of droplet breakup in liquid–liquid dispersions by CFD–PBM simulations: The influence of the surfactant type. Chinese J. Chem. Eng. 25, 1369–1380. https://doi.org/10.1016/J.CJCHE.2017.01.014

Li, D., Gao, Z., Buffo, A., Podgorska, W., Marchisio, D.L., 2017b. Droplet breakage and coalescence in liquid-liquid dispersions: Comparison of different kernels with EQMOM and QMOM. AIChE J. 63, 2293–2311. https://doi.org/10.1002/aic.15557

Liao, Y., Lucas, D., 2010. A literature review on mechanisms and models for the coalescence process of fluid particles. Chem. Eng. Sci. 65, 2851–2864. https://doi.org/10.1016/j.ces.2010.02.020

Liao, Y., Lucas, D., 2009. A literature review of theoretical models for drop and bubble breakup in turbulent dispersions. Chem. Eng. Sci. 64, 3389–3406. https://doi.org/10.1016/j.ces.2009.04.026

Maaß, S., Paul, N., Kraume, M., 2012. Influence of the dispersed phase fraction on experimental and predicted drop size distributions in breakage dominated stirred systems. Chem. Eng. Sci. 76, 140–153. https://doi.org/10.1016/j.ces.2012.03.050

Maluta, F., Montante, G., Paglianti, A., 2020. Analysis of immiscible liquid-liquid mixing in stirred

tanks by Electrical Resistance Tomography. Chem. Eng. Sci. 227, 115898. https://doi.org/10.1016/j.ces.2020.115898

Marchisio, D.L., Fox, R.O., 2013. Computational Models for Polydisperse Particulate and Multiphase Systems, Cambridge University Press. Cambridge University Press, Cambridge. https://doi.org/10.1017/CBO9781139016599

Montante, G., Horn, D., Paglianti, A., 2008. Gas–liquid flow and bubble size distribution in stirred tanks. Chem. Eng. Sci. 63, 2107–2118. https://doi.org/10.1016/j.ces.2008.01.005

Montante, G., Paglianti, A., Magelli, F., 2012. Analysis of dilute solid–liquid suspensions in turbulent stirred tanks. Chem. Eng. Res. Des. 90, 1448–1456. https://doi.org/10.1016/j.cherd.2012.01.009

Mukherjee, S., Safdari, A., Shardt, O., Kenjereš, S., Van den Akker, H.E.A., 2019. Droplet–turbulence interactions and quasi-equilibrium dynamics in turbulent emulsions. J. Fluid Mech. 878, 221–276. https://doi.org/10.1017/jfm.2019.654

Narsimhan, G., Gupta, J.P., Ramkrishna, D., 1979. A model for transitional breakage probability of droplets in agitated lean liquid-liquid dispersions. Chem. Eng. Sci. 34, 257–265. https://doi.org/10.1016/0009-2509(79)87013-X

Passalacqua, A., Fox, R.O., 2011. Implementation of an iterative solution procedure for multi-fluid gas-particle flow models on unstructured grids. Powder Technol. 213, 174–187. https://doi.org/10.1016/j.powtec.2011.07.030

Podgórska, W., 2005. Scale-up effects in coalescing dispersions—comparison of liquid–liquid systems differing in interface mobility. Chem. Eng. Sci. 60, 2115–2125.

https://doi.org/10.1016/j.ces.2004.10.035

Podgórska, W., Bałdyga, J., 2001. Scale-up effects on the drop size distribution of liquid–liquid dispersions in agitated vessels. Chem. Eng. Sci. 56, 741–746. https://doi.org/10.1016/S0009-2509(00)00284-0

Rieger, R., Weiss, C., Wigley, G., Bart, H.-J., Marr, R., 1996. Investigating the process of liquid-liquid extraction by means of computational fluid dynamics. Comput. Chem. Eng. 20, 1467–1475. https://doi.org/10.1016/0098-1354(95)00232-4

Roache, P.J., 1998. Verification and Validation in Computational Science and Engineering. Hermosa Publishers, Albuquerque, New Mexico.

Sciacchitano, A., Wieneke, B., 2016. PIV uncertainty propagation. Meas. Sci. Technol. 27, 084006. https://doi.org/10.1088/0957-0233/27/8/084006

Sharp, K. V., Adrian, R.J., 2001. PIV study of small-scale flow structure around a Rushton turbine. AIChE J. 47, 766–778. https://doi.org/10.1002/aic.690470403

Shiea, M., Buffo, A., Vanni, M., Marchisio, D., 2020. Numerical Methods for the Solution of Population Balance Equations Coupled with Computational Fluid Dynamics. Annu. Rev. Chem. Biomol. Eng. 11, 339–366. https://doi.org/10.1146/annurev-chembioeng-092319-075814

Solsvik, J., Skjervold, V.T., Han, L., Luo, H., Jakobsen, H.A., 2016. A theoretical study on drop breakup modeling in turbulent flows: The inertial subrange versus the entire spectrum of isotropic turbulence. Chem. Eng. Sci. 149, 249–265. https://doi.org/10.1016/j.ces.2016.04.037

Soos, M., Kaufmann, R., Winteler, R., Kroupa, M., Lüthi, B., 2013. Determination of maximum

turbulent energy dissipation rate generated by a rushton impeller through large eddy simulation. AIChE J. 59, 3642–3658. https://doi.org/10.1002/aic.14206

Tang, Q., Ye, S., Wang, Y., Liu, Z., 2018. A study on liquid-liquid dispersions in a continuous mixer via computational fluid dynamics (CFD) simulation combined with population balance model (PBM). Can. J. Chem. Eng. 97, cjce.23361. https://doi.org/10.1002/cjce.23361

Triballier, K., Dumouchel, C., Cousin, J., 2003. A technical study on the Spraytec performances: influence of multiple light scattering and multi-modal drop-size distribution measurements. Exp. Fluids 35, 347–356. https://doi.org/10.1007/s00348-003-0674-1

Vejražka, J., Zedníková, M., Stanovský, P., 2018. Experiments on breakup of bubbles in a turbulent flow. AIChE J. 64, 740–757. https://doi.org/10.1002/aic.15935

Vonka, M., Soos, M., 2015. Characterization of liquid-liquid dispersions with variable viscosity by coupled computational fluid dynamics and population balances. AIChE J. 61, 2403–2414. https://doi.org/10.1002/aic.14831

Wang, C.Y., Calabrese, R. V., 1986. Drop breakup in turbulent stirred-tank contactors. Part II: Relative influence of viscosity and interfacial tension. AIChE J. 32, 667–676. https://doi.org/10.1002/aic.690320417

Yeoh, S.L., Papadakis, G., Yianneskis, M., 2004. Numerical Simulation of Turbulent Flow Characteristics in a Stirred Vessel Using the LES and RANS Approaches with the Sliding/Deforming Mesh Methodology. Chem. Eng. Res. Des. 82, 834–848. https://doi.org/10.1205/0263876041596751

Yoon, H.S., Balachandar, S., Ha, M.Y., Kar, K., 2003. Large Eddy Simulation of Flow in a Stirred

Tank. J. Fluids Eng. 125, 486–499. https://doi.org/10.1115/1.1566046

Zhang, J., Xu, S., Li, W., 2012. High shear mixers: A review of typical applications and studies on power draw, flow pattern, energy dissipation and transfer properties. Chem. Eng. Process. Process Intensif. 57–58, 25–41. https://doi.org/10.1016/j.cep.2012.04.004

Zhou, G., Kresta, S.M., 1998a. Evolution of drop size distribution in liquid–liquid dispersions for various impellers. Chem. Eng. Sci. 53, 2099–2113. https://doi.org/10.1016/S0009-2509(97)00437-5

Zhou, G., Kresta, S.M., 1998b. Correlation of mean drop size and minimum drop size with the turbulence energy dissipation and the flow in an agitated tank. Chem. Eng. Sci. 53, 2063–2079. https://doi.org/10.1016/S0009-2509(97)00438-7